Visualization of depletion layer in AlGaN homojunction p–n junction

Kengo Nagata[1, 2*], Satoshi Anada[3], Yoshiki Saito[2], Maki Kushimoto[1], Yoshio Honda[4], Tetsuya Takeuchi[5], Kazuo Yamamoto[3], Tsukasa Hirayama [3, 4], and Hiroshi Amano[4]

[1]*Graduate School of Engineering, Nagoya University, Furo-cho, Chikusa-ku, Aichi 464-8603, Japan*

[2]*Toyoda Gosei Co., Ltd., 710 Shimomiyakeoriguchi, Heiwa-cho, Inazawa, Aichi 290-1312, Japan*

[3]*Nanostructure Research Laboratory, Japan Fine Ceramics Center, 2-4-1 Mutsuno, Atsuta-ku, Nagoya, Aichi 456-8587, Japan*

[4]*Center for Integrated Research of Future Electronics, Institute of Materials and Systems for Sustainability, Nagoya University, Furo-cho, Chikusa-ku, Nagoya, Aichi 464-8601, Japan*

[5]*Faculty of Science and Technology, Meijo University, 1-501 Shiogamaguchi, Tempaku-ku, Nagoya, Aichi 468-8502, Japan*

[*]E-mail: nagata.kengo@c.mbox.nagoya-u.ac.jp, kengo.nagata@toyoda-gosei.co.jp

We analyzed the p–n junction of an aluminum gallium nitride (AlGaN) homojunction tunnel junction (TJ) deep-ultraviolet light-emitting diode by phase-shifting electron holography. We clearly obtained a phase image reflecting the band alinement of the p–n homojunction and derived a depletion layer width of approximately 10 nm. In addition, the observed depletion layer width for the AlGaN TJ was in good agreement with the simulated one reflecting the diffusion profile of Mg and Si, thus enabling a discussion on the electrical conduction mechanism for an AlGaN p-n junction.

Aluminum gallium nitride (AlGaN)-based deep-ultraviolet (UV) light-emitting diodes (LEDs) can be controlled to emit light having a specific wavelength in the range of 210–365 nm by changing the Al composition of light-emitting AlGaN layers. The deep-UV LEDs are desired to replace mercury lamps for skin treatment, resin curing, and sterilization 1–3). However, the wall plug efficiency (WPE) of commercial deep-UV LEDs has remained less than 5 % 4–9). This is mainly because they have a p-type GaN cladding layer that undesirably absorbs deep-UV light, resulting in extremely low light extraction efficiency (LEE). To achieve high LEE for the deep-UV LEDs, such absorbing layers must be substituted by fully transparent device structures in the deep-UV region; AlGaN tunnel junctions (TJs) with high Al compositions have been regarded as a promising structure 10–12). However, the operating voltages of AlGaN TJ LEDs are still high because our understanding of the electrical conduction mechanism is insufficient for AlGaN TJs and the device structural design has not yet been completely optimized. Some of the causes of the high operating voltages have been considered to be as follows: high resistivity in the p$^+$-type AlGaN and n$^+$-type AlGaN of the TJ due to self-compensation by, for example, cation-vacancy–Si (V_{III}–nSi) ($n = 1$ to 3) complexes, Mg inversion domains, and nitrogen vacancies (V_N^{3+}) 13-18); and low tunneling probability for the AlGaN TJ due to the thick depletion layer at the AlGaN TJ, which is caused by high ionization energies of dopants for both n-type and p-type AlGaN. The depletion layer is closely related to nanoscale or atomic-scale electric properties such as electric potential and charge density distributions. Visualizing the electric potential and charge densities enables us to understand the electric conduction mechanism of the TJ layer in greater detail and to optimize the TJ structure more efficiently. Therefore, to reduce the operating voltage of AlGaN TJ deep-UV LEDs, it is important to assess the local electric properties of the AlGaN p–n junction with high spatial resolution. Although dopant distributions in a p–n junction can commonly be evaluated by secondary ion mass spectrometry (SIMS), its spatial resolution is not sufficiently high to analyze the AlGaN TJ in detail. Moreover, SIMS cannot be used to evaluate the extent to which dopants are not ionized, not activated or compensated for by some defects. One of the most effective methods for local electric characterization is electron holography (EH), a transmission electron microscopy (TEM) technique, with which one can directly obtain an electric potential distribution at the nanometer scale. EH has been used to measure the potential of semiconductor structures, such as GaAs and GaN p–n junctions 19–21). In this work, we measure the electric potential and derive the depletion layer width for the $Al_{0.6}Ga_{0.4}N$ homojunction TJ by phase-shifting EH (PS-EH), which can simultaneously achieve high precision and high spatial resolution 22–25). Besides that, we compare the depletion layers obtained by PS-EH and band simulation to discuss the electrical conduction mechanism for the AlGaN TJ.

An AlGaN homojunction TJ deep-UV LED was grown by low-pressure metalorganic vapor phase epitaxy (MOVPE) on 4-inch flat (0001) sapphire substrates with a miscut angle of 0.35° toward the sapphire $[11\bar{2}0]$ direction. The AlN nucleation layer was grown at a surface temperature of 1100 °C, and a 3-μm-thick layer was subsequently grown at a surface temperature of 1270 °C. A 1.3-μm-thick n-type $Al_{0.6}Ga_{0.4}N$ underlayer doped with 3×10^{19} cm^{-3} Si was grown on the AlN template17, 18). The growth of the n-type AlGaN underlayer was followed by that of second-period multi–quantum wells (MQWs) consisting of 11-nm-thick Si-doped n-type $Al_{0.55}Ga_{0.45}N$ barriers and 2-nm-thick $Al_{0.45}Ga_{0.55}N$ wells, then a Mg-doped p-type $Al_{0.85}Ga_{0.15}N$ electron-blocking layer, 50-nm-thick p-type $Al_{0.6}Ga_{0.4}N$, 50-nm-thick p^{+}-type $Al_{0.6}Ga_{0.4}N$ with 1.5×10^{20} cm^{-3} Mg, 40-nm-thick n^{+}-type $Al_{0.6}Ga_{0.4}N$ with 1. 8×10^{20} cm^{-3} Si, and a 250-nm-thick n-type $Al_{0.6}Ga_{0.4}N$ contact layer. The device structure is shown in Fig. 1 a). The electrical characteristics of bulk samples were described in ref. 12. The $Al_{0.6}Ga_{0.4}N$ homojunction TJ deep-UV LEDs showed an operating voltage of 10.8 V and a WPE of 0.7 % at 63 A/cm^2. A sample for PS-EH was extracted from the anode-side electrode and thinned using a cryo-FIB system (Hitachi NB5000) operated at an accelerating voltage of 40 kV and a low temperature of 120 K, by which thermal damage during ion milling can be reduced. The FIB direction was perpendicular to the p–n junction. Then, the surface damage layers were reduced using Ga-ion beams with lower voltages in the range of 5–20 kV at a sample temperature of 120 K. A sample with a smooth surface and a uniform thickness of 350 nm is obtained. After depositing carbon, the flat plate region in the sample was observed vertically with the device structure by EH TEM (Hitachi HF-3300EH) with a cold field emission gun operated at 300 kV. A double-biprism optical system was used to prevent Fresnel fringes in the electron-interference fringe pattern (hologram), as shown in Fig. 1 b)26–28). Holograms are formed by the interference of an object wave modulated by a sample with a reference wave passing through vacuum, recorded digitally using a chargecoupled device camera (Gatan UltraScan 4000). Subsequently, the holograms are used to reproduce the phase of the object wave reflecting the electric potential of the sample. The spatial resolution is 1.8 nm. The hologram must be commonly recorded under the off-Bragg condition in the observation region by adjusting the sample tilt. In this study, the sample was tilted by 0.7° from the direction parallel to the TJ interface. Each interface of the layers in this TEM image is blurred by approximately ± 4 nm. Figure 2 (Legends: black lines) shows an ideal equilibrium band diagram and the charge density profile of an $Al_{0.6}Ga_{0.4}N$ homojunction TJ LED calculated by SiLENSe29) using the simulation parameters of Mg and Si impurities that were intentionally doped into each layer. The charge densities of the p-type and n-type sides in the TJ were the same as the dopant concentrations, 1.5×10^{20} cm^{-3} and 1.7×10^{20} cm^{-3}, respectively; that is, all dopants act as electric charges near the AlGaN p-n junction. The calculated thickness of the depletion layer was 4 nm. Figures 3 a), b), and c) show the TJ layer structure, a cross-sectional TEM image of the $Al_{0.6}Ga_{0.4}N$ homojunction TJ, and a hologram in the same region, respectively. The TEM image (Fig. 3 b)) shows no contrast arising from the interface of the AlGaN TJ with the same Al composition. We confirmed that the Al compositions of both the p^+-type AlGaN and n^+-type AlGaN layers are also approximately 60 % by point-by-point correction–secondary ion mass spectrometry (PCOR–SIMS), as shown in Fig. 3 d). In the hologram (Fig. 3 c)), the interference fringes bend at the interface between the p^+- and n^+-type AlGaN layers. A one-dimensional phase profile reconstructed from the hologram (Fig. 3 c)) are shown in Fig. 3 e). The phase in the n^+-type AlGaN layer shifts as it comes closer to the TJ interface, which means that the electric potential increases. On the other hand, the p^+-type AlGaN layer shows the lowest phase near the TJ interface. The phase difference shows an electric potential difference between the p^+-type and n^+-type AlGaN layers27, 30). Thus, each AlGaN layer has a polarity corresponding to the dopants, and the phase profile (Fig. 3 e)) well matched the SIMS profile (Fig. 3 d)). Figure 4 shows the electric potential profile and charge density in the AlGaN homojunction TJ, calculated using the phase profile and the following equations:

$$\Delta\phi = \frac{\pi}{\lambda E}\Delta V t, \qquad (1)$$

$$Q = -\varepsilon\frac{d^2\Delta V}{d^2 t}, \qquad (2)$$

where $\Delta\phi$, ΔV, Q, λ, E, t, and ε are the phase difference, potential difference, charge density, wavelength of electron wave, acceleration voltage, active layer thickness, and dielectric constant, respectively. The phase profile (Fig. 3 e)) was converted to the potential and charge density profiles (Fig. 4)) by assuming that the potential difference between the p^+-type and n^+-type AlGaN layers is the built-in potential of 4.8 eV for AlGaN with an Al composition of 60 %, where t was 57.5 nm and the bowing parameter of $Al_xGa_{1-x}N$ was 1 eV 31). The value of t was smaller than the sample thickness because of surface depletion and damage caused by FIB processing 32–34). From the potential profile (Fig. 4), the depletion layer width was measured to be approximately 10 nm at the AlGaN TJ interface, which was thicker than the calculated one in Fig. 2. Here, we defined the depletion layer width as the distance between the maximum and minimum potential points in the potential profile (Fig. 4)). From the charge density profile (Fig. 4), both of the charge densities in the p^+-type and n^+-type AlGaN layers at the TJ interface were measured to be approximately 1.1×10^{20} cm^{-3}, which were lower than those in Fig. 2. To discuss the results of PS-EH, we performed a more practical band simulation reflecting the impurity profiles by SiLENSe. Figure 2 (Legends: red lines) shows the simulated equilibrium band diagram and the charge density profile of the $Al_{0.6}Ga_{0.4}N$ homojunction TJ, reflecting the Mg and Si diffusion profiles obtained by P-COR SIMS. From the band simulation, the depletion layer width was calculated to be 10 nm, which is consistent with that measured by PS-EH. The simulated result indicates that the depletion layer is widened by carrier compensations due to the diffusion of both Mg and Si in the AlGaN homojunction TJ and suggests that the carrier compensations occurred in the actual TJ in the present AlGaN TJ LED sample. The simulated electric charge densities in the p^+-type and n^+-type AlGaN layers were 5.0×10^{19} cm^{-3} and 7.7×10^{19} cm^{-3}, respectively, which are lower than those measured by PS-EH. This discrepancy between the simulated and measured charge densities may be due to the inadequate measurement precision. Since the noise in the measured electric potential profile was amplified by differentiation (Eq. (2)), the resulting charge density profile was noisy, as shown in Fig. 4. To measure the charge densities more accurately, the precision of PS-EH must be improved. We also observed positive and negative charge spikes of $7–8 \times 10^{19}$ cm^{-3} in the p^+-AlGaN side shown in Fig. 4, arising from the electric potential valley; such charge spikes do not look like artifacts. Although these charge spikes may be caused by dopant segregation near the TJ interface, the origin is currently unclear. In the future, we will attempt to suppress impurity diffusions at the TJ using better growth techniques, such as low-temperature growth, to obtain TJs with a narrower depletion layer and to reduce the operating voltage. In addition, we will optimize the doping concentration in the AlGaN TJ since the p^+-type/n^+-type AlGaN layers are strongly affected by self-compensations. 13-18)

In summary, we analyzed the electric potential of AlGaN homojunction TJ deep-UV LEDs by PS-EH. We directly measured the depletion layer width in the $Al_{0.6}Ga_{0.4}N$ homojunction TJ to be approximately 10 nm. The measured depletion layer width was in good agreement with that calculated by the band simulation for the AlGaN homojunction TJ reflecting the impurity profiles, which suggests the importance of suppressing impurity diffusions in the TJ. We also found that the precision of the present PS-EH is not sufficiently high to correctly measure the charge densities in the AlGaN TJ. These results indicate that PS-EH can provide important and unique information on nanoscale electric properties in the AlGaN homojunction TJ deep-UV LEDs and will be made more useful by improving its measurement precision by, for example, using a direct detection camera and/or machine learning image processing. 27, 35, 36)

ACKNOWLEDGMENTS

This work was supported by MEXT "Research and development of next-generation semiconductor to realize energy-saving society" Program Grant Number JPJ005357. This work was the result of using research equipment shared in MEXT Project for promoting public utilization of advanced research infrastructure (Program for supporting introduction of the new sharing system) Grant Number JPMXS0410500120.

References

1) K. Oguma, S. Rattanakul, and M. Masaike, Water Supply **19**, 1507 (2019).

2) H. Inagaki, A. Saito, H. Sugiyama, T. Okabayashi, and S. Fujimoto, Emerging Microbes Infect. **9**, 1744 (2020).

3) Y. Saito, S. Wada, K. Nagata, H. Makino, S. Boyama, H. Miwa, S. Matsui, K. Kataoka, T. Narita, and K. Horibuchi, Jpn. J. Appl. Phys. **60,** 080501 (2021).

4) M. Ichikawa, A. Fujioka, T. Kosugi, S. Endo, H. Sagawa, H. Tamaki, T. Mukai, M. Uomoto, and T. Shimatsu, Appl. Phys. Express **9**, 072101 (2016).

5) T. Takano, T. Mino, J. Sakai, N. Noguchi, K. Tsubaki, and H. Hirayama, Appl. Phys. Express **10**, 031002 (2017).

6) M. Shatalov, W. Sun, A. Lunev, X. Hu, A. Dobrinsky, Y. Bilenko, J. Yang, M. Shur, R. Gaska, and C. Moe, Appl. Phys. Express **5**, 082101 (2012).

7) T. Inazu, S. Fukahori, C. Pernot, M. H. Kim, T. Fujita, Y. Nagasawa, A. Hirano, M. Ipponmatsu, M. Iwaya, T. Takeuchi, S. Kamiyama, M. Yamaguchi, Y. Honda, H. Amano, and I. Akasaki, Jpn. J. Appl. Phys. **50**, 122101 (2011).

8) Y. J. Sung, M. S. Kim, H. Kim, S. Choi, Y. H. Kim, M. H. Jung, R. J. Choi, Y. T. Moon, J. T. Oh, H. H. Jeong, and G. Y. Yeom, Opt. Express **27**, 29930 (2019).

9) S. Y. Lee, D. S. Han, Y. G. Lee, K. K. Choi, J. T. Oh, H. H. Jeong, T. Y. Seong, and H. Amano, ECS J. Solid State Sci. Technol. **9**, 065016 (2020).

10) V. Fan Arcara, B. Damilano, G. Feuillet, S. Vézian, K. Ayadi, S. Chenot, and J.-Y. Duboz, J. Appl. Phys. **126**, 224503 (2019).

11) E. A. Clinton, Z. Engel, E. Vadiee, J. V. Carpenter, Z. C. Holman, and W. A. Doolittle, Appl. Phys. Lett. **115**, 082104 (2019).

12) K. Nagata, H. Makino, H. Miwa, S. Matsui, S. Boyama, Y. Saito, M. Kushimoto, Y. Honda, T. Takeuchi, and H. Amano, Appl. Phys. Express **14** 084001 (2021).

13) M. L. Nakarmi, K. H. Kim, M. Khizar, Z. Y. Fan, J. Y. Lin, and H. X. Jiang, Appl. Phys. Lett. **86**, 092108 (2005).

14) T. Kinoshita, T. Obata, H. Yanagi, and S. Inoue, Appl. Phys. Lett. **102**, 012105 (2013).

15) I. Bryan, Z. Bryan, S. Washiyama, P. Reddy, B. Gaddy, B. Sarkar, M. H. Breckenridge, Q. Guo, M. Bobea, J. Tweedie, S. Mita, D. Irving, R. Collazo, and Z. Sitar, Appl. Phys. Lett. **112**, 062102 (2018).

16) J. S. Harris, J. N. Baker, B. E. Gaddy, I. Bryan, Z. Bryan, K. J. Mirrielees, P. Reddy, R. Collazo, Z. Sitar, and D. L. Irving, Appl. Phys. Lett. **112**, 152101 (2018).

17) K. Nagata, H. Makino, T. Yamamoto, K. Kataoka, T. Narita, and Y. Saito, Appl. Phys. Express **13**, 025504 (2020).

18) K. Kataoka, T. Narita, K. Nagata, H. Makino, and Y. Saito, Appl. Phys. Lett. **117**, 262103 (2020).

19) S. Anada, K. Yamamoto, H. Sasaki, N. Shibata, Y. Hori, K. Kinugawa, A. Imamura, and T. Hirayama, J. Appl. Phys. **122**, 225702 (2017).

20) S. Neugebauer, M. P. Hoffmann, H. Witte, J. Bläsing, A. Dadgar, A. Strittmatter, T. Niermann, M. Narodovitch, and M. Lehmann, Appl. Phys. Lett. **110**, 102104 (2017).

21) S. Anada, K. Yamamoto, H. Sasaki, N. Shibata, M. Matsumoto, Y. Hori, K. Kinugawa, A. Imamura, and T. Hirayama, Microscopy **68**, 159 (2019).

22) Q. Ru, J. Endo, T. Tanji, and A. Tonomura, Appl. Phys. Lett. **59**, 2372 (1991).

23) Q. Ru, G.L. Lai, K. Aoyama, J. Endo, and A. Tonomura, Ultramicroscopy **55**, 209 (1994).

24) K. Yamamoto, I. Kawajiri, T. Tanji, M. Hibino, and T. Hirayama, J. Electron Microsc. **49**, 31 (2000).

25) K. Yamamoto, T. Hirayama, and T. Tanji, Ultramicroscopy **101**, 265 (2004).

26) K. Harada, A. Tonomura, Y. Togawa, T. Akashi, and T. Matsuda, Appl. Phys. Lett. **84**, 3229 (2004).

27) M. R. McCartney, D. J. Smith, R. Hull, J. C. Bean, E. Voelkl, and B. Frost, Appl. Phys. Lett. **65**, 2603 (1994).

28) K. Yamamoto, I. Kawajiri, T. Tanji, M. Hibino, and T. Hirayama, J. Electron Microsc. **49**, 31 (2000).

29) SiLENSe–software tool for LED bandgap engineering (https://www.str-soft.com/devices/silense/)

30) F. Yun, M. A. Reshchikov, L. He, T. King, and H. Morkoç, J. Appl. Phys. **91**, 9856 (2002).

31) F. Yun, M. A. Reshchikov, L. He, T. King, and H. Morkoç, J. Appl. Phys. **92**, 4837 (2002).

32) T. Sato, K. Nakano, H. Matsumoto, S. Torikawa, I. Nakatani, M. Kiyohara, and T.

Isshiki, J. Phys.: Conf. Ser. **902** 012019 (2017).

33) W. D. Rau, P. Schwander, F. H. Baumann, W. Höppner, and A. Ourmazd, Phys. Rev. Lett. **82** 2614 (1999).

34) Z. Wang, T. Hirayama, K. Sasaki, H. Saka, and N. Kato, Appl. Phys. Lett. **80**, 246 (2002).

35) S. L. Y. Chang, C. Dwyer, J. Barthel, C. B. Boothroyd, R. E. Dunin-Borkowski, Ultramicroscopy **161** 90 (2016).

36) S. Anada, Y. Nomura, T. Hirayama, K. Yamamoto, Ultramicroscopy **206**, 112818 (2019).

Figure Captions

Fig. 1. a) Device structure of $Al_{0.6}Ga_{0.4}N$ homojunction TJ deep-UV LED. b) Schematic diagram of the optical system in the TEM for double-biprism PS-EH.

Fig. 2. Equilibrium band diagrams and the charge density profiles of $Al_{0.6}Ga_{0.4}N$ homojunction TJ layer calculated by SiLENSe. Regarding the red line, the diffusion of impurities Mg and Si was added to the simulation parameters of Mg and Si in the SIMS profile. The depletion layer widths are defined as the distance between the maximum and minimum charge density points (black and red arrows).

Fig. 3. PS-EH observation of $Al_{0.6}Ga_{0.4}N$ homojunction TJ deep-UV LED sample. a) Layer structure of AlGaN homojunction TJ deep-UV LED, b) cross-sectional TEM image of AlGaN homojunction TJ deep-UV LED, c) electron-interference fringe pattern (hologram) in region a), d) SIMS profile across layers, and e) phase profile across layers.

Fig. 4. Electric potential profile of $Al_{0.6}Ga_{0.4}N$ homojunction TJ layer calculated from phase profile (Fig. 3 e)).

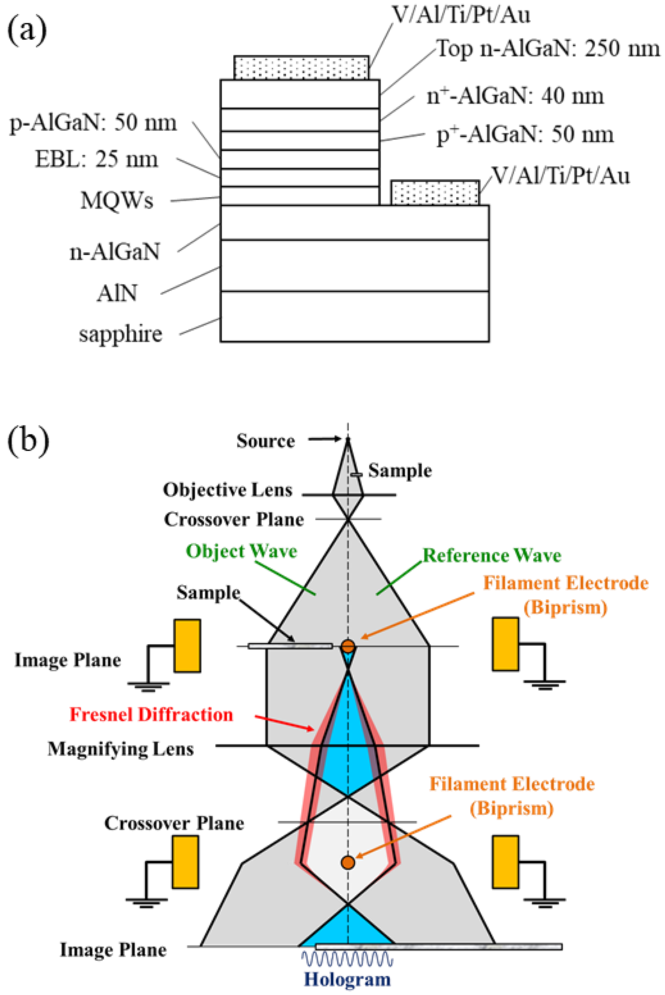

Fig. 1. (Color)
Color print
(Single column)

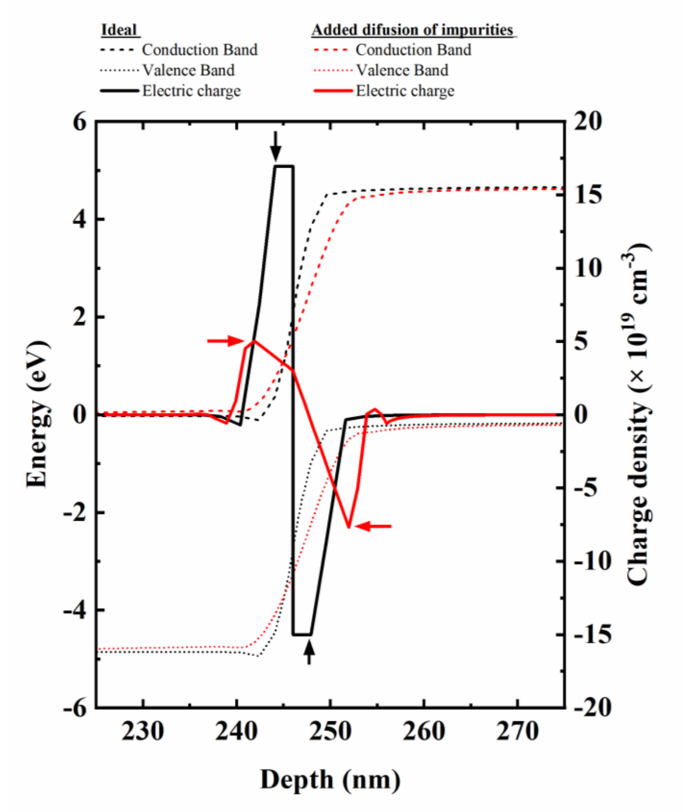

Fig. 2. (Color)

Color print

(single column)

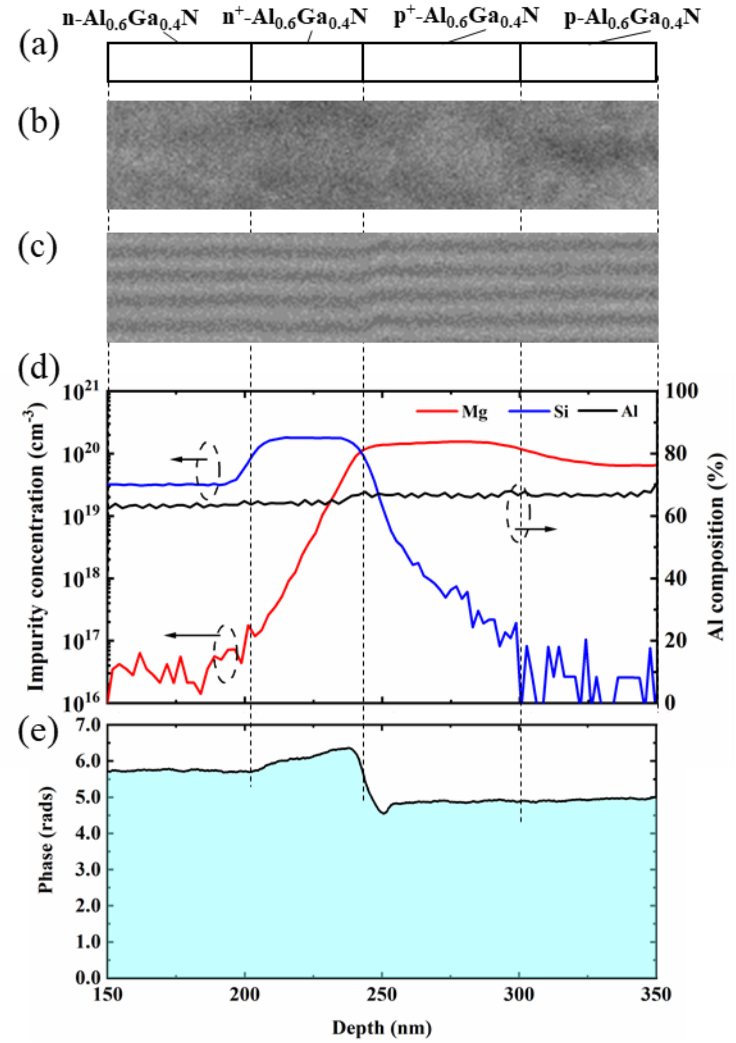

Fig. 3. (Color)

Color print

(single column)

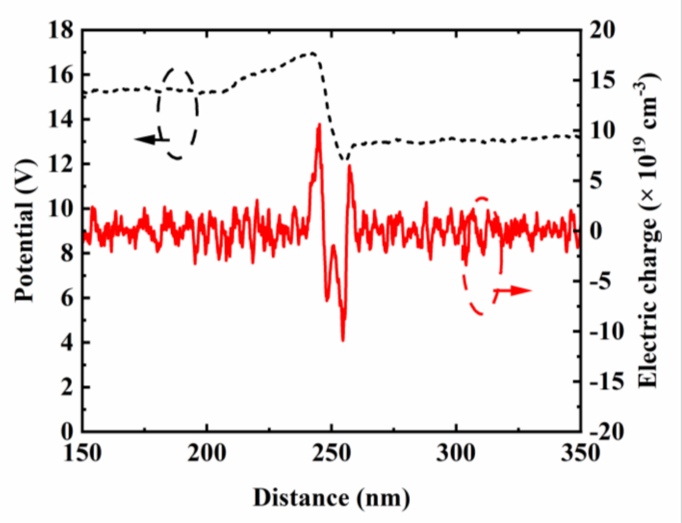

Fig. 4. (Color)

Color print

(single column)